H1prelim-08-012 Submitted to

XVI International Workshop on Deep Inelastic Scattering, DIS 2008 April 7-11, 2008, London
Parallel Session **Diffraction and Vector Mesons**

Electronic Access: www-h1.desy.de/h1/publications/H1preliminary.short_list.html

Diffractive photoproduction of dijets in ep collisions at HERA

H1 Collaboration

Abstract

Two measurements are presented of differential dijet cross sections in diffractive photoproduction ($Q^2 < 0.01$ GeV^2) based on 1999 and 2000 HERA data with integrated luminosity of 54 pb^{-1}. The event topology is given by $ep \to eXY$, where the system X, containing at least two jets, is separated from a leading low-mass proton dissociative system Y by a large rapidity gap. The measurements are made in two kinematic ranges differing primarily in the transverse energy requirements on the two hardest jets. The dijet cross sections are compared with next-to-leading order QCD predictions based on recent diffractive parton densities obtained by H1. The next-to-leading order calculations predict larger cross sections than the data. The suppression of the data relative to the calculation is found to have no significant dependence on the photon four-momentum fraction entering the hard subprocess. There is a suggestion of a dependence of the suppression factor on the transverse energy of the jets.

1 Introduction

In this document two measurements are presented of differential dijet cross sections in the photoproduction regime of *ep* scattering. In photoproduction two basic leading order (LO) classes of photon interactions exist - direct and resolved. In the direct processes the photon interacts as a point-like particle. In the resolved processes the photon can develop its structure and acts as a composite particle. In diffractive ep scattering the proton stays intact or dissociates into a low-mass ($M_Y \ll E_{cm}$) state. The hard diffractive processes can be considered as an exchange of a vacuum quantum number object (Pomeron, $I\!P$). A large gap in the rapidity distribution of the final state hadrons is observed. Owing to the photon structure there is an apparent resemblance between the resolved photoproduction and the hadron-hadron scattering. The factorization of the QCD calculable subprocess from the diffractive parton distribution functions (DPDF) in proton is not expected to hold in the hadron-hadron collisions [1]. The additional photon remnant and proton interactions are expected to fill the large rapidity gap and, therefore, to spoil the experimental signature of the diffractive event. Such a mechanism is expected to explain the difference between the measured structure function extracted from dijet production rates in $p\bar{p}$ collisions at Tevatron and the theoretical predictions based on the diffractive parton densities by H1 [2].

The measurements are based on luminosity of 54 pb^{-1} which is about a factor of three larger than previous H1 measurement in similar kinematic domain [3].

2 Theory and Models

2.1 Motivation

Previous results concerning two jet production in diffractive photoproduction presented by the H1 and ZEUS collaborations can be found in [3] and [4], respectively. In [3] an overall suppression factor of 0.5 is applied to the NLO theory prediction in order to reproduce the measured cross section. In [4] a similar analysis is presented with somewhat higher E_T range required on the jets. In [4] the global suppression factor of the NLO theory predictions ranges from about 0.6 to 0.9, within the errors - depending on the DPDFs used.

In [3, 4] lack of dependence of the suppression factors are observed on the photon four-momentum fraction (x_γ) entering the hard subprocess. In both papers harder E_T^{jet1} differential cross section spectra are observed in the data than in the NLO theory prediction. This observation, though not very significant, indicates that there may be a dependence of the suppression factor on the E_T range of the jets. Under these circumstances, the original H1 analysis [3] was performed also in the second cut scheme in order to approach the analysis phase space from [4] as closely as possible.

2.2 The Kinematics

In figure 1 (a) and (b) examples of a direct and resolved diffractive production of two jets are shown, respectively.

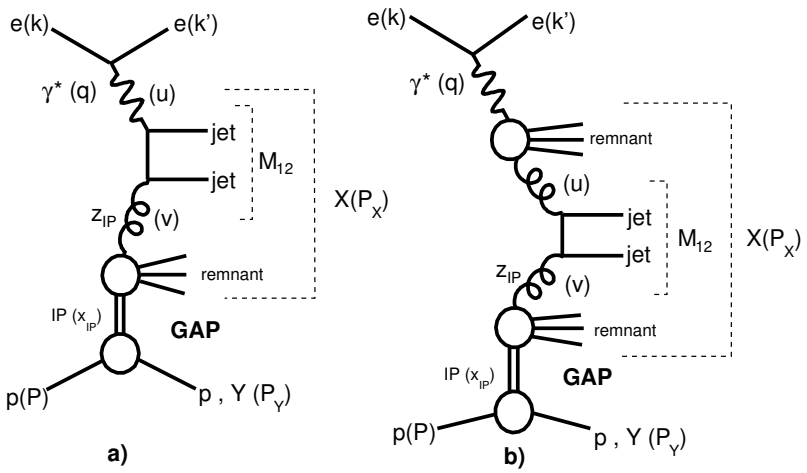

Figure 1: Leading order diagrams for diffractive dijet photoproduction at HERA. Diagrams (a) and (b) represent the direct and resolved photon interactions, respectively. The diffractive exchange is labeled with $I\!P$.

The kinematics can be described in terms of the following invariants

$$s \equiv (k+P)^2, \quad Q^2 \equiv -q^2, \quad y \equiv \frac{q.P}{k.P}, \quad x \equiv \frac{Q^2}{2\,q.P}, \tag{1}$$

where the four-vectors are defined according to figure 1.

These variables are standard DIS variables and are related through $Q^2 \approx s\,x\,y$, where s is the square of the total CMS energy of the collision, Q^2 is the photon virtuality, y is the scattered electron inelasticity and x is the four-momentum fraction of the proton transfered to the interaction. Furthermore, the invariant mass of the photon-proton system is given by

$$W \equiv \sqrt{(q+P)^2} \approx \sqrt{ys - Q^2}. \tag{2}$$

Using the notation from figure 1 diffraction specific variables can be defined as

$$M_X \equiv P_X^2, \quad M_Y \equiv P_Y^2, \quad t \equiv (P - P_Y)^2, \quad x_{I\!P} \equiv \frac{q.(P - P_Y)}{q.P}, \tag{3}$$

where M_X and M_Y are the invariant masses of the diffractive and proton dissociative systems, respectively, t is the four momentum transfer squared at the proton vertex and $x_{I\!P}$ is the four-momentum fraction of the proton transferred to the system X.

With u and v being the four-momenta of photon and parton (parton and parton) in direct (resolved) processes entering the hard subprocess the invariant dijet mass can be expressed as

$$M_{12} \equiv \sqrt{(u+v)^2}. \tag{4}$$

Finally, the longitudinal four-momentum fractions of the photon and the diffractive exchange transferred to the hard interaction can be defined as

$$x_\gamma \equiv \frac{P.u}{P.q}, \quad z_{I\!P} \equiv \frac{q.v}{q.(P - P_Y)}. \tag{5}$$

The jets are obtained using the k_T longitudinally invariant jet algorithm in the laboratory frame [5].

The first measurement is performed in the kinematic range

$$\begin{aligned} Q^2 &< 0.01 \text{ GeV}^2, && (6)\\ 0.3 &< y < 0.65, && (7)\\ E_T^{jet1} &> 5 \text{ GeV}, && (8)\\ E_T^{jet2} &> 4 \text{ GeV}, && (9)\\ -1 &< \eta^{jet1,\,jet2} < 2, && (10)\\ x_{I\!P} &< 0.03, && (11)\\ |t| &< 1 \text{ GeV}^2, && (12)\\ M_Y &< 1.6 \text{ GeV}, && (13) \end{aligned}$$

where E_T^{jet1} and η^{jet1} are the transverse energy and pseudorapidity of the leading jet, respectively, both in the laboratory frame. The same notation applies to the sub-leading jet.

The second measurement differs from the above kinematics in following items

$$\begin{aligned} E_T^{jet1} &> 7.5 \text{ GeV}, && (14)\\ E_T^{jet2} &> 6.5 \text{ GeV}, && (15)\\ -1.5 &< \eta^{jet1,\,jet2} < 1.5, && (16)\\ x_{I\!P} &< 0.025. && (17)\\ & && (18) \end{aligned}$$

It therefore matches the kinematic range of [4] except that it has a more restrictive y and Q^2 ranges and different treatment of proton dissociation contribution.

The kinematics are reconstructed according to following formulae.

$$\begin{aligned} y &= y_e = 1 - \frac{E_{e'}}{E_e^{beam}}, && (19)\\ W &= \sqrt{s\, y_e}, && (20)\\ x_\gamma &= \frac{\Sigma_{jets} E_i - P_{z,i}}{\Sigma_{HFS} E_i - P_{z,i}}, && (21)\\ x_{I\!P} &= \frac{\Sigma_{HFS} E_i + P_{z,i}}{2.E_p^{beam}}, && (22)\\ z_{I\!P} &= \frac{\Sigma_{jets} E_i + P_{z,i}}{2.x_{I\!P}.E_p^{beam}}, && (23)\\ M_{12} &= \sqrt{J^{(1),\mu}.J_\mu^{(2)}}, && (24)\\ M_X &= \sqrt{s\, y_e\, x_{I\!P}}, && (25)\\ \left|\Delta\eta^{jets}\right| &= \left|\eta^{jet1} - \eta^{jet2}\right|, && (26)\\ \left\langle \eta^{jets} \right\rangle &= \frac{1}{2}\left(\eta^{jet1} + \eta^{jet2}\right). && (27) \end{aligned}$$

Where, E_e^{beam} and E_p^{beam} are the lepton and proton beam energies, respectively. The $E_{e'}$ is the scattered electron energy. The $J^{(1)\mu}$ and $J_\mu^{(2)}$ are the four vector components of the jets.

2.3 NLO QCD calculations

There are two independent NLO programs in this analysis used to predict the measured cross sections; the Frixione et al. (FR) program [6] and the Klasen & Kramer (KK) program [7]. The NLO QCD predictions were obtained setting the renormalization and factorization scales to $\mu_r = \mu_f = E_T^{Jet1}$ with fixed number of flavours $N_f = 5$ and $\Lambda_5 = 0.228$. The DPDF fits obtained by H1 are used; H1 2006 Fit A and Fit B DPDF [8] and H1 2007 Fit Jets DPDF, which can be found in [9]. For the resolved photon, the $\gamma-$PDF parameterization GRV HO [10] is used. The non-perturbative transition to the level of stable hadrons is included in the predictions by means of hadronization corrections obtained from the Rapgap Monte Carlo simulation (see section 2.4).

2.4 Monte Carlo simulations

The signal dijet events are generated in the range $Q^2 < 0.01$ GeV^2 and $\hat{p}_T^{min} > 2$ GeV [1] with the Rapgap Monte Carlo (MC) generator [11] using the H1 2006 fit B DPDFs both for direct and resolved processes and for Pomeron and meson exchange. The photon structure function is GRV-G LO [10]. The signal samples are used for correction of the data to the hadron level and for calculation of the hadronization corrections.

The hadronization corrections are calculated in each bin of the observables as a ratio of cross sections at the hadron level to the parton level in the MC sample.

$$(1 + \delta_{hadr.})_i = \left(\frac{\sigma_{dijet}^{hadron}}{\sigma_{dijet}^{parton}} \right)_i , \tag{28}$$

where i denotes the measured bin.

In order to estimate the non-diffractive background contribution the Pythia MC generator [12] is used in photoproduction mode.

3 Experimental Procedure

3.1 H1 detector

A detailed description of the H1 detector can be found in [13]. Here, only a brief account on the detector components relevant to the present analysis is given.

The *ep* interaction point in H1 is surrounded by silicon strip detectors followed, among other components, by two layers of large concentric drift chambers for charged particle tracking. The chambers cover a pseudorapidity region of $-1.5 < \eta < 1.5$ with a resolution of $\sigma(P_T)/P_T = 0.005 P_T/GeV \oplus 0.015$. The chambers are also designed to provide triggering information. The central tracking detectors are surrounded by a LAr calorimeter covering $-1.5 < \eta < 3.4$

[1] ... and $\hat{p}_T^{min} > \sqrt{5}$ GeV for the second cut scheme analysis.

measuring with resolution of $\sigma/E = 0.11/\sqrt{E/GeV}$ in its electromagnetic part and $\sigma/E = 0.50/\sqrt{E/GeV}$ in the hadronic part. The above mentioned devices are placed inside a large superconducting solenoid producing a magnetic field of 1.16 T. The backward region $-4 < \eta < 1.4$ is covered by a lead-scintillating fiber calorimeter (SpaCal).

The luminosity is measured by means of Bethe-Heitler processes $ep \to ep\gamma$ with the use of a luminosity system which consists of a photon detector and electron detectors.

An efficient non-photoproduction background suppression can be achieved by means of use of a crystal Čerenkov calorimeter at ~ -33 m from the interaction point for the scattered electron tagging.

In the forward region the H1 detector is equipped with the Forward Muon Detector (FMD) and the Proton Remnant Tagger (PRT). They are efficiently used for tagging of the rapidity gap events together with the cut on the most forward cluster in the LAr calorimeter. Hence we measure a contribution of proton dissociative processes.

3.2 Event selection

The data collected by H1 in 1999 and 2000 nominal vertex running period with an e^+ beam are analyzed. The proton and positron nominal beam energies are 920 GeV and 27.5 GeV, respectively.

The positron is tagged in the electron tagger at -33 m from the interaction point. The overlap of Bethe-Heitler processes is suppressed by means of a cut on energy in the photon lumi-detector.

The diffractive event selection is based on the large rapidity gap method using a cut on the pseudorapidity ($\eta^{max} < 3.2$) of most forward cluster in the LAr (with energy $E^{clus.} > 400$ MeV) together with an absence of signal in the PRT and a cut on the activity above noise level in the FMD. In addition, a cut on $x_{I\!P}$ is applied as the diffractive events mostly contribute at low $x_{I\!P}$ values ($x_{I\!P} \sim 0.05$ and lower). Such a selection does not ensure a purely elastic proton in the final state. Eventually, the cross sections are corrected to the phase scape of the elastic proton and the proton dissociation of $M_Y < 1.6$ GeV and $|t| < 1$ GeV^2.

The hadronic final state is measured in the central tracker chambers and the calorimeters. The jets are formed from the final state objects by means of the k_T longitudinally invariant algorithm [5] in the laboratory frame ($R = 1$ and $p_T^{jet,min} > 2.5$ GeV). The asymmetric cuts on the transverse energies of the jets are chosen to facilitate the comparison with the NLO calculations.

About 4960 and 560 events survive the event selection in the "low" and "high" E_T^{jet} schemes, respectively.

3.3 Cross section measurement and systematic uncertainties

The differential cross section is measured in each bin i of variable x by means of formula

$$\left(\frac{d\sigma}{dx}\right)_i = \frac{N_i^{data}/\varepsilon_i^{trigg.} - N_i^{MC,bgd.}}{A_i\,\Delta_i^x\,L} \cdot \frac{1}{C^{p.diss.}}. \quad (29)$$

The meaning of the quantities in (29) is as follows: $N_i^{data}/\varepsilon_i^{trigg.}$ is the number of detected events corrected for trigger inefficiency, $N_i^{MC,bgd.}$ is the background fraction obtained from Monte Carlo simulation, A_i is the correction factor to the level of stable hadrons (accounting on acceptance and smearing) calculated from MC (with an average value of 0.31), Δ_i^x is the bin width, L is the luminosity of the data and finally $C^{p.diss.}$ [$C^{p.diss.} = 0.94 \pm 7\%(syst.)$], obtained from MC, accounts for the correction into the range (12) and (13).

The systematic uncertainties are evaluated for all significant sources and are presented together with the data. In both analyses they are dominated by the hadronic final state energy scale uncertainty, the inefficiency of the LRG selection, the proton dissociation correction factor and the correction factors A_i.

4 Results

Preliminary H1 results are presented for both analyses. First is presented the measurement in the original H1 cut scheme (denoted as $E_T^{jet1} > 5$ GeV and $E_T^{jet2} > 4$ GeV). Next is presented the analysis restricted to larger transverse momenta ($E_T^{jet1} > 7.5$ GeV and $E_T^{jet2} > 6.5$ GeV) [2].

4.1 $E_T^{jet1} > 5$ GeV and $E_T^{jet2} > 4$ GeV

The NLO calculations (FR and KK) predict larger cross sections than the data. The overall suppression factors of the NLO calculations needed in order to predict the total measured cross section depend mainly on the DPDF set used. There is very good agreement between FR and KK for both the total and the differential cross sections. The total measured cross section (σ_{tot}^{data}) and the suppression factors (S) are listed below.

$$\sigma_{tot}^{data} = 305.4 \text{ pb} \pm 5.6(stat.) \pm 54.4(syst.), \quad (30)$$
$$S_{fitB}^{FR} = 0.54 \pm 0.01(stat.) \pm 0.10(syst.)^{+0.14}_{-0.13}(scale.), \quad (31)$$
$$S_{fitB}^{KK} = 0.51 \pm 0.01(stat.) \pm 0.10(syst.), \quad (32)$$
$$S_{fitA}^{FR} = 0.43 \pm 0.01(stat.) \pm 0.10(syst.), \quad (33)$$
$$S_{fitJets}^{FR} = 0.65 \pm 0.01(stat.) \pm 0.11(syst.), \quad (34)$$

where size of the renormalization scale uncertainty from (31) can be expected to be similar in (32), (33) and (34).

[2] Although, the difference between the analyses rests also in the η range of the jets and the $x_{I\!P}$ range only the E_T ranges will be used to distinguish between them.

In figure 2 the measurement is presented of the differential cross section as a function of E_T^{jet1}. The statistical and uncorrelated systematic uncertainties are added in quadrature and are represented with error bars (inner is statistical only). The correlated uncertainties are shown separately with a dark band. The FR and KK NLO calculations based on Fit B are multiplied by the hadronization correction factors (shown underneath) and are multiplied by a common scale factor of 0.53. The NLO calculations are always shown for the central renormalization scale ($\mu_r = E_T^{jet1}$). Predictions are also presented for FR Fit B with renormalization scale variations ($\mu_r/2$ and $2.\mu_r$) depicted as a band around the central FR Fit B values. In the lower part of figure 2 ratios of the measured differential cross sections in the data to the predictions is presented (data/theory). No scaling factors are applied to the NLO predictions in this case. The ratio is shown for the FR Fit B calculation with correspondingly propagated uncertainties stemming from the data. Also the renormalization scale variations of the ratio are presented for FR Fit B. Ratios with respect to the FR Fit A and FR Fit Jets calculations are also shown in order to illustrate the approximative DPDF uncertainty. The variations due the DPDF uncertainties are of order of renormalization scale variations of FR Fit B. In a similar way the results are presented for $z_{I\!P}$, x_γ and $\log_{10}(x_{I\!P})$ in figures 3, 4 and 5, respectively.

In figure 2 a somewhat harder $d\sigma/dE_T^{jet1}$ slope is measured in data than is predicted by both NLO calculations. Consequently the ratio (data/theory) in the same figure shows a suggestion of a weaker suppression as E_T^{jet1} increases. Taking into account all uncertainties considered the value of the ratio for $E_T^{jet1} < 7$ GeV is roughly within a range of $0.3 - 0.7$. In contrast for $E_T > 7$ GeV the ratio lies in the range $0.4 - 1$.

In figure 3 a good description of the measured $d\sigma/dz_{I\!P}$ is provided by Fit B. Therefore, the ratio of data to theory is flat for FR Fit B. It is also almost independent of DPDF at low $z_{I\!P}$. However, for larger $z_{I\!P}$ the DPDF uncertainty increases dramatically. The hatched area in the last $z_{I\!P}$ bin in the figure 3 indicates that the results are presented beyond the range of the DPDF fits. The H1 2006 Fit A and B are valid for $z_{I\!P} < 0.8$ and the H1 2007 Fit Jets is valid for $z_{I\!P} < 0.9$, [8, 9].

In figure 4 a very good description is obtained of the measured $d\sigma/dx_\gamma$ shape by Fit B. From the data to theory ratio in figure 4 it can be deduced that there is no significant x_γ dependence of the suppression in contrast to expectations [1] but in agreement with previous results [3, 4]. The variations due the DPDF uncertainties are of similar size to the scale variations of FR Fit B.

In figure 5 a very good description of the $d\sigma/dlog_{10}(x_{I\!P})$ shape is provided by Fit B. The measured ratio in figure 5 is consistent with independence of $x_{I\!P}$. The variations due the DPDF uncertainties are of similar size to the scale variations of FR Fit B.

4.2 $E_T^{jet1} > 7.5$ GeV and $E_T^{jet2} > 6.5$ GeV

In the higher E_T^{jet} range, the NLO calculations (FR and KK) predict larger cross sections than the data again. The total measured cross section and the factors by which the NLO calculations

exceed the data are listed below.

$$\sigma_{tot}^{data} = 37 \text{ pb} \pm 2(stat.) \pm 8(syst.), \quad (35)$$
$$S_{fitB}^{FR} = 0.61 \pm 0.03(stat.) \pm 0.13(syst.)^{+0.16}_{-0.14}(scale.), \quad (36)$$
$$S_{fitB}^{KK} = 0.62 \pm 0.03(stat.) \pm 0.14(syst.), \quad (37)$$
$$S_{fitA}^{FR} = 0.44 \pm 0.02(stat.) \pm 0.09(sst.), \quad (38)$$
$$S_{fitJets}^{FR} = 0.79 \pm 0.04(stat.) \pm 0.16(syst.). \quad (39)$$

In general the suppression factors decrease with respect to the full E_T range analysis (see section 4.1). The FR Fit B and KK Fit B calculations are presented with a common suppression factor of 0.61 applied to the differential cross section comparisons in figures 6 - 14.

In figure 6 the $d\sigma/dE_T^{jet1}$ shape is in reasonable agreement with the FR and KK Fit B calculations. This is reflected in the ratio in figure 6 where the ${E_T}^{jet1}$ dependence cannot be independently verified but is not excluded. The variations of the ratio allowed within the uncertainties show that the suppression is in the range off to 0.9 in the first two E_T^{jet1} bins.

In figure 7 FR and KK predictions based on Fit B are able to describe the measured $d\sigma/dz_{I\!P}$ shape taking into account the large uncertainties. In the ratio plot again a large DPDF uncertainty is observed at high $z_{I\!P}$ values. The hatching in the last $z_{I\!P}$ bin indicates that the fits are used beyond the fit range, see section 4.1.

In figure 8 both Fit B NLO predictions manage to reproduce the shape of the $d\sigma/dx_\gamma$. Within the precision of the analysis the ratio is independent of x_γ.

In figures 9 - 14 the results are presented for $x_{I\!P}$, W, $|\eta^{jets}|$, $\langle\eta^{jets}\rangle$, M_X and M_{12}, respectively. Given the large uncertainties the shapes are described by the FR and KK Fit B predictions. Fluctuations due to low statistics in some bins are observed in the ratios.

5 Discussion and Conclusions

Differential cross sections are measured for diffractive dijet photoproduction in two phase space regions with H1 data. The measured cross sections are compared with next-to-leading order QCD predictions based on three sets of diffractive parton distribution functions. Also the ratios of the measured differential cross sections to the predicted differential cross sections are studied.

In the analysis with lower E_T cuts on the jets the FR NLO calculation based on the H1 2006 Fit B DPDF overestimates the data. A global suppression factor of 0.54 ± 0.01(stat.)± 0.10(syst.)$^{+0.14}_{-0.13}$ (scale.) is measured. The lack of any significant x_γ dependence of the data/theory ratio is consistent with the previous H1 result [3]. The Klasen & Kramer calculation based on the H1 2006 Fit B DPDF gives consistent results with the predictions obtained by Frixione et al. program. There is a suggestion of a dependence of the suppression factor on the E_T of the jets. In the region of $E_T^{jet1} < 7$ GeV the suppression is consistent with previous H1 measurement [3]. Weakening suppression is suggested for the range of $E_T^{jet1} > 7$ GeV which leads to suppression factors which are consistent with a previous result of the ZEUS collaboration [4]. A large sensitivity of the results to the diffractive parton distribution functions is observed in all variables

through comparisons with the H1 2006 Fit A and H1 2007 Fit Jets DPDFs. The variations due to different fits are similar in size to the renormalization scale variations of the Fit B calculation arising dominantly for the large $z_{I\!P}$ region.

Indeed, in the analysis with the higher E_T of the jets a weaker suppression factor of $0.61 \pm 0.03(\text{stat.}) \pm 0.13(\text{syst.})^{+0.16}_{-0.14}$ (scale.) is measured for the FR NLO calculation based on the H1 2006 Fit B DPDF. The lack of a significant x_γ dependence of the data/theory ratio is consistent with the result of the ZEUS collaboration [4]. Further dependence of suppression factor on the E_T^{jet1} is still not excluded but cannot be independently verified. Taking the uncertainties into account including the DPDF fit variations the suppression remains consistent with that presented in [4].

Acknowledgements

We are grateful to the HERA machine group whose outstanding efforts have made this experiment possible. We thank the engineers and technicians for their work in constructing and maintaining the H1 detector, our funding agencies for financial support, the DESY technical staff for continual assistance and the DESY directorate for support and for the hospitality which they extend to the non DESY members of the collaboration.

We would like to express our gratitude to M. Klasen. We appreciate a lot his efforts concerning the NLO QCD calculations which allowed us an independent verification of the results.

References

[1] A.Kaidalov *et al.*, *Phys.Lett.* **B559** (2003) 235-238.

[2] T. Affolder *et al.* [CDF Collaboration], Diffractive Dijets with a Leading Antiproton in $\bar{p}p$ Collisions at $\sqrt{s}$ = 1800 GeV, *Phys. Rev. Lett.* **84** (2000) 5043

[3] A. Aktas *et al.* [H1 Collaboration], Tests of QCD factorization in the diffractive production of dijets in deep-inelastic scattering and photoproduction at HERA, *Eur.Phys.J.* **C51** (2007) 549-568.

[4] S. Chekanov *et al.* [ZEUS Collaboration], Diffractive Photoproduction of Dijets in ep Collisions at HERA, (2007) submitted to *Europ. Phys. Journal C*.

[5] S.Catani, Yu.L. Dokshitzer, B.R. Webber, *Phys. Lett.* **B285** (1992) 291.

[6] S.Frixione, Z.Kunzst and A.Signer, *Nucl. Phys.* **B467** (1996) 399 [hep-ph/9512328];
S.Frixione, *Nucl. Phys.* **B507** (1997) 295 [hep-ph/9706545];
see also http://www.ge.infn.it/∼ridolfi/.

[7] M. Klasen and G. Kramer it Eur. Phys. J. **C38** (2004.) 93.

[8] A. Aktas *et al.* [H1 Collaboration], Measurement and QCD Analysis of the Diffractive Deep-Inelastic Scattering Cross Section at HERA, *Eur. Phys. J.* **C48** (2006) 715-748.

[9] A. Aktas *et al.* [H1 Collaboration], Dijet Cross Sections and Parton Densities in Diffractive DIS at HERA, *JHEP* (2007) 0710:042

[10] M. Glück, E. Reya and A. Vogt, *Phys. Rev.* **D 45** (1992) 3986;
M. Glück, E. Reya and A. Vogt, *Phys. Rev.* **D 46** (1992) 1973.

[11] H. Jung, *Comp. Phys. Comm.* **86**, (1995) 147.

[12] T. Sjöstrand, *Comp. Phys. Comm.* **82** (1994) 74;
T. Sjöstrand, High energy physics event generation with PYTHIA 5.7 and JETSET 7.4, *CERN TH/7111-93* (1993, rev. 1994).

[13] I. Abt *et al.* [H1 Collaboration], *Nucl. Instrum. Methods* **A386** (1997) 310-347.

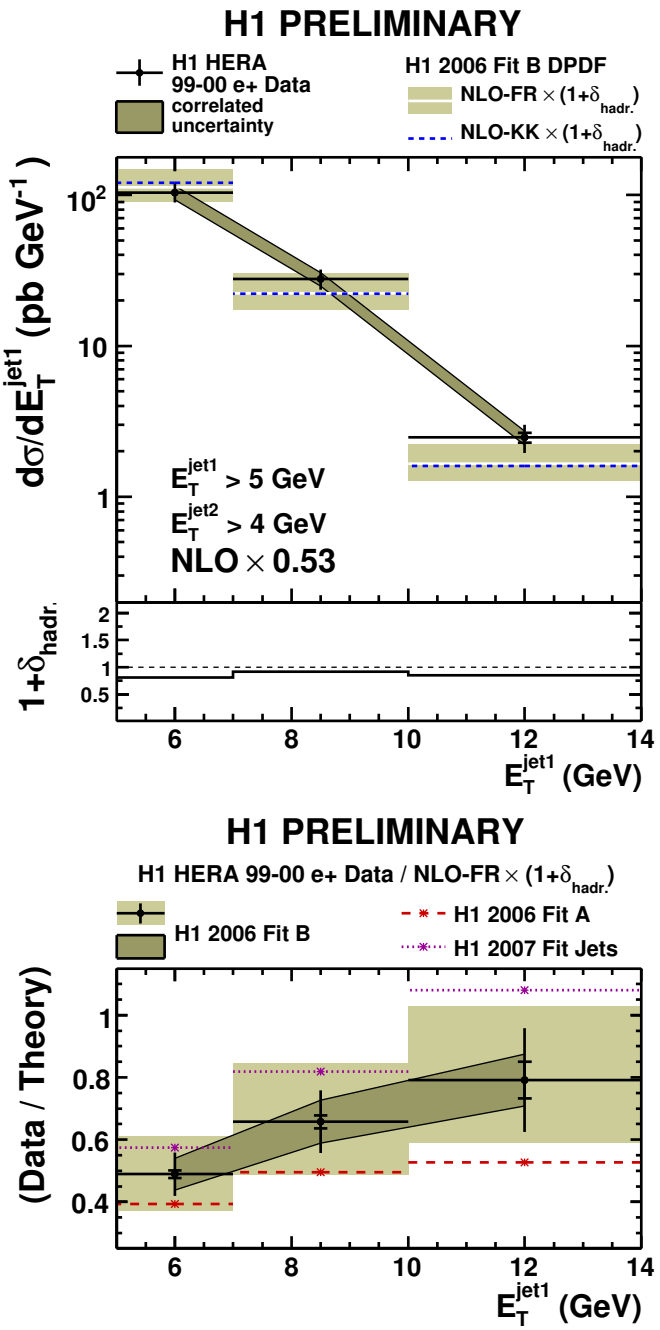

Figure 2: Upper plot: measurement of the differential cross section $\mathrm{d}\sigma/\mathrm{d}E_T^{jet1}$. The points show the data, the inner error bars on the points are statistical and the outer error bars show statistical and uncorrelated uncertainties added in quadrature. The correlated systematic errors are indicated by the dark band. The data are compared with predictions based on the H1 2006 Fit B DPDFs, scaled by a constant factor of 0.53, obtained using the FR (white line) and KK (dashed line) calculations. Both predictions are corrected for hadronisation effects using the factor $(1+\delta_{hadr})$ shown below the main figure. The effect on the FR calculation of varying μ_r by factors of 0.5 and 2.0 is shown in the light band. Lower plot: ratio of the measured differential cross section to the FR calculation based on the H1 2006 Fit B DPDF set and corrected for hadronisation effects. The experimental and theory scale uncertainties are indicated as for the cross section plot. Also indicated are the central values obtained when the H1 2006 Fit A or H1 2007 Fit Jets DPDFs are used in place of H1 2006 Fit B.

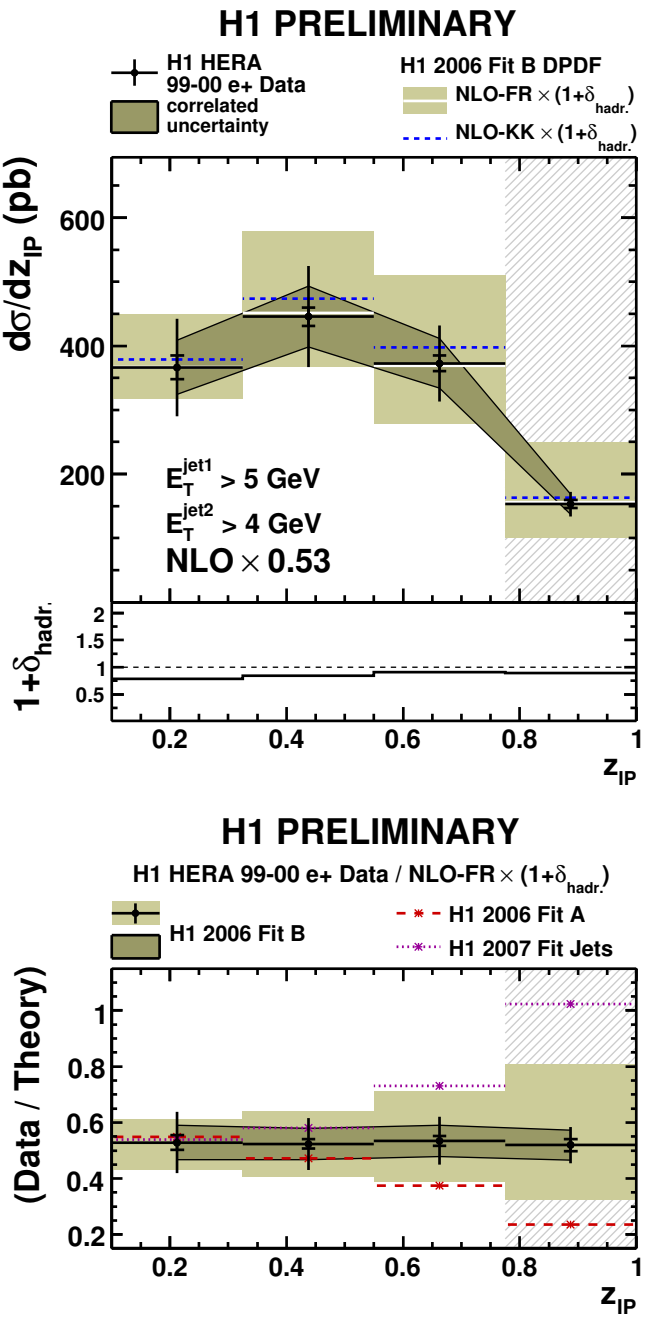

Figure 3: Upper plot: measurement of the differential cross section $\mathrm{d}\sigma/\mathrm{d}z_{I\!P}$. The points show the data, the inner error bars on the points are statistical and the outer error bars show statistical and uncorrelated uncertainties added in quadrature. The correlated systematic errors are indicated by the dark band. The data are compared with predictions based on the H1 2006 Fit B DPDFs, scaled by a constant factor of 0.53, obtained using the FR (white line) and KK (dashed line) calculations. Both predictions are corrected for hadronisation effects using the factor $(1 + \delta_{hadr})$ shown below the main figure. The effect on the FR calculation of varying μ_r by factors of 0.5 and 2.0 is shown in the light band. Lower plot: ratio of the measured differential cross section to the FR calculation based on the H1 2006 Fit B DPDF set and corrected for hadronisation effects. The experimental and theory scale uncertainties are indicated as for the cross section plot. Also indicated are the central values obtained when the H1 2006 Fit A or H1 2007 Fit Jets DPDFs are used in place of H1 2006 Fit B.

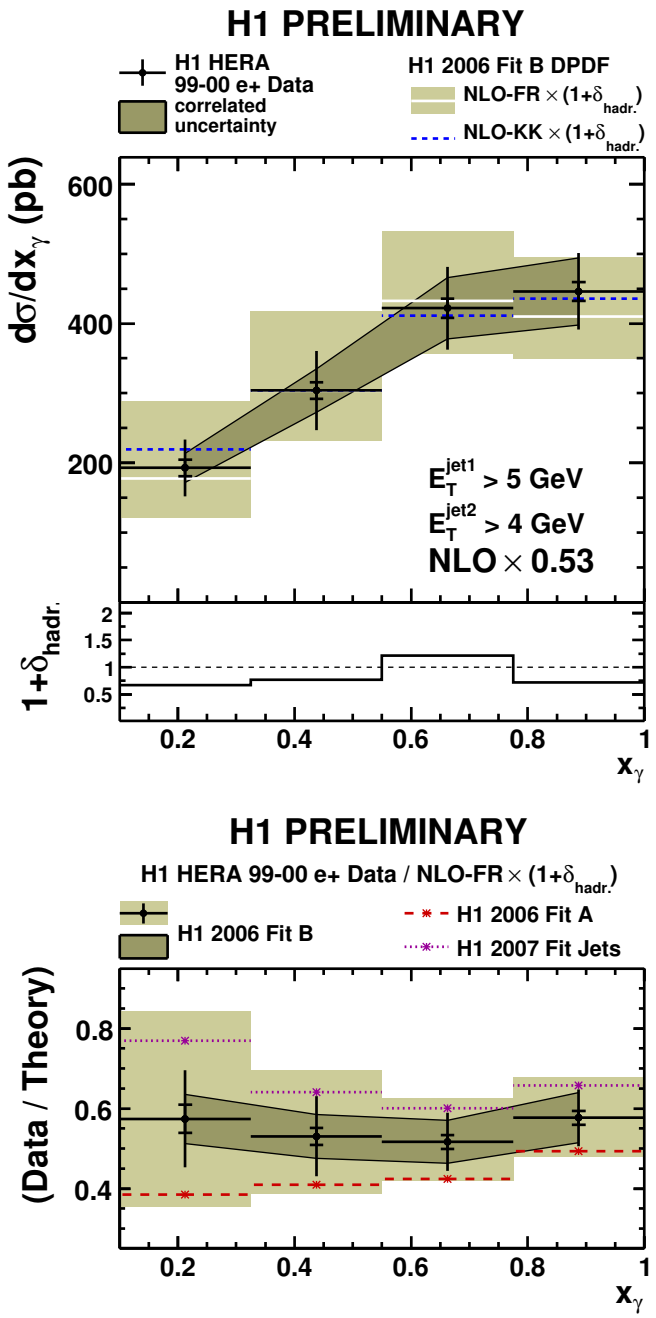

Figure 4: Upper plot: measurement of the differential cross section $\mathrm{d}\sigma/\mathrm{d}x_\gamma$. The points show the data, the inner error bars on the points are statistical and the outer error bars show statistical and uncorrelated uncertainties added in quadrature. The correlated systematic errors are indicated by the dark band. The data are compared with predictions based on the H1 2006 Fit B DPDFs, scaled by a constant factor of 0.53, obtained using the FR (white line) and KK (dashed line) calculations. Both predictions are corrected for hadronisation effects using the factor $(1 + \delta_{hadr})$ shown below the main figure. The effect on the FR calculation of varying μ_r by factors of 0.5 and 2.0 is shown in the light band. Lower plot: ratio of the measured differential cross section to the FR calculation based on the H1 2006 Fit B DPDF set and corrected for hadronisation effects. The experimental and theory scale uncertainties are indicated as for the cross section plot. Also indicated are the central values obtained when the H1 2006 Fit A or H1 2007 Fit Jets DPDFs are used in place of H1 2006 Fit B.

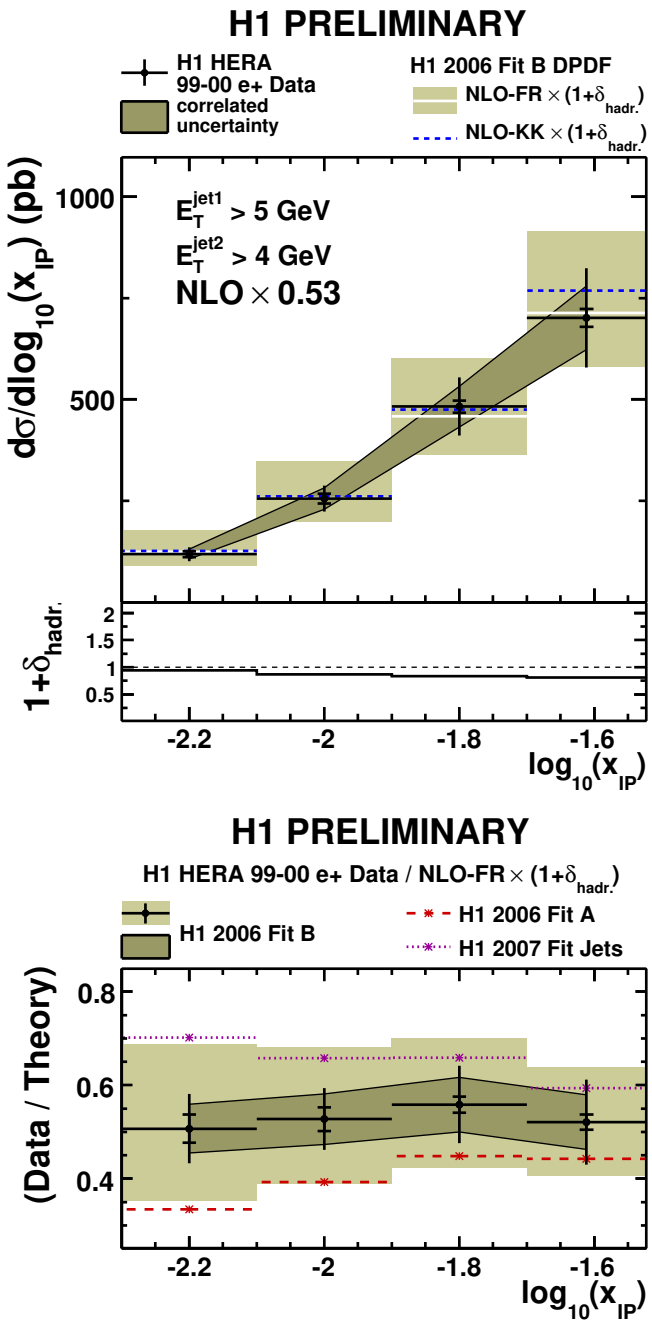

Figure 5: Upper plot: measurement of the differential cross section $\mathrm{d}\sigma/\mathrm{d}log_{10}(x_{I\!P})$. The points show the data, the inner error bars on the points are statistical and the outer error bars show statistical and uncorrelated uncertainties added in quadrature. The correlated systematic errors are indicated by the dark band. The data are compared with predictions based on the H1 2006 Fit B DPDFs, scaled by a constant factor of 0.53, obtained using the FR (white line) and KK (dashed line) calculations. Both predictions are corrected for hadronisation effects using the factor $(1+\delta_{hadr})$ shown below the main figure. The effect on the FR calculation of varying μ_r by factors of 0.5 and 2.0 is shown in the light band. Lower plot: ratio of the measured differential cross section to the FR calculation based on the H1 2006 Fit B DPDF set and corrected for hadronisation effects. The experimental and theory scale uncertainties are indicated as for the cross section plot. Also indicated are the central values obtained when the H1 2006 Fit A or H1 2007 Fit Jets DPDFs are used in place of H1 2006 Fit B.

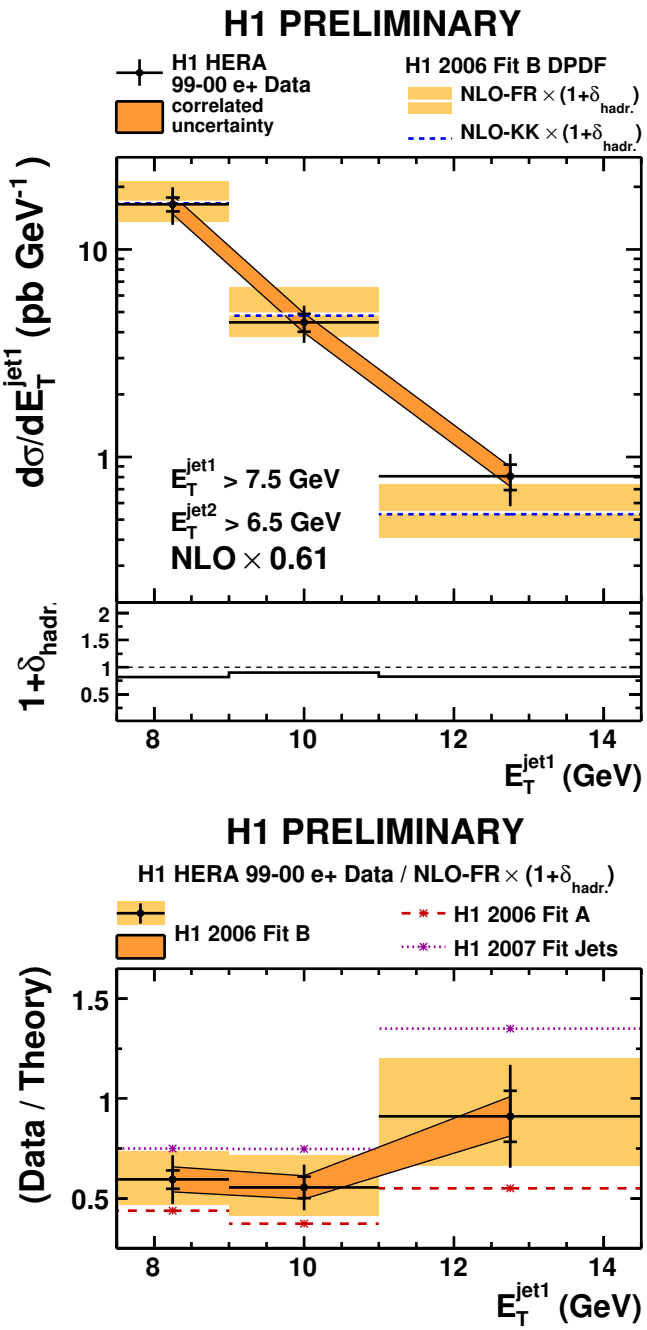

Figure 6: Upper plot: measurement of the differential cross section $\mathrm{d}\sigma/\mathrm{d}E_T^{jet1}$. The points show the data, the inner error bars on the points are statistical and the outer error bars show statistical and uncorrelated uncertainties added in quadrature. The correlated systematic errors are indicated by the dark band. The data are compared with predictions based on the H1 2006 Fit B DPDFs, scaled by a constant factor of 0.61, obtained using the FR (white line) and KK (dashed line) calculations. Both predictions are corrected for hadronisation effects using the factor $(1+\delta_{hadr})$ shown below the main figure. The effect on the FR calculation of varying μ_r by factors of 0.5 and 2.0 is shown in the light band. Lower plot: ratio of the measured differential cross section to the FR calculation based on the H1 2006 Fit B DPDF set and corrected for hadronisation effects. The experimental and theory scale uncertainties are indicated as for the cross section plot. Also indicated are the central values obtained when the H1 2006 Fit A or H1 2007 Fit Jets DPDFs are used in place of H1 2006 Fit B.

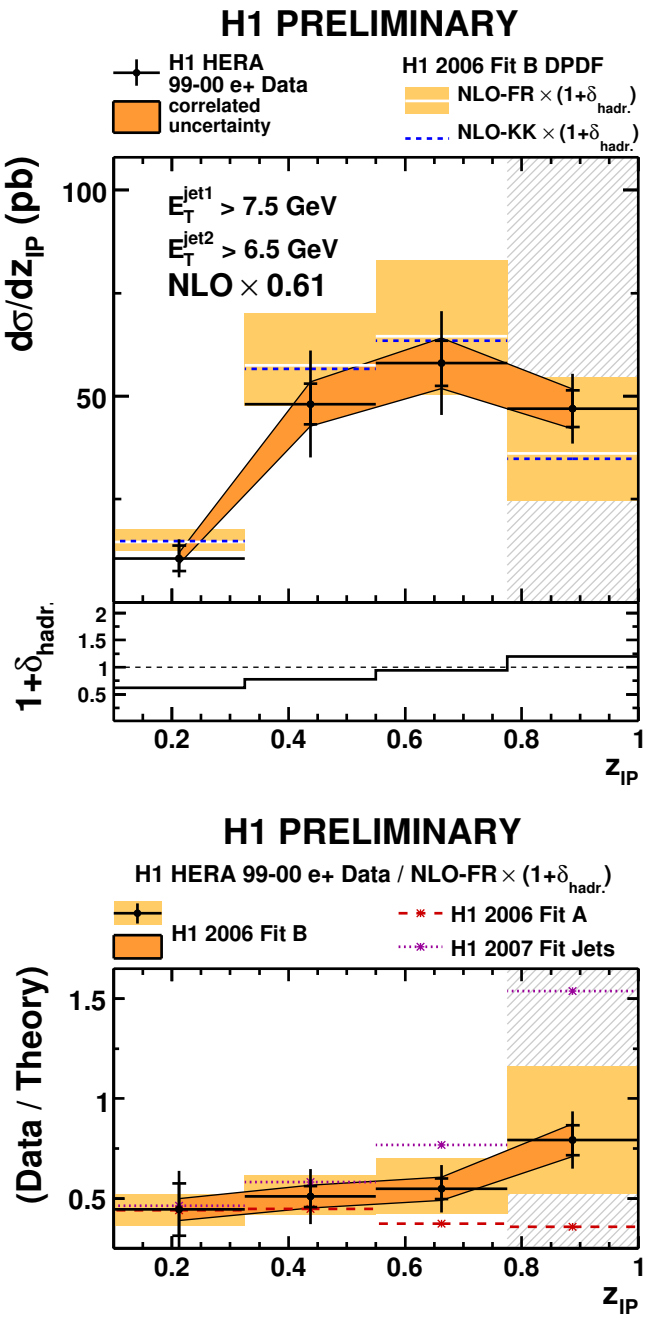

Figure 7: Upper plot: measurement of the differential cross section $\mathrm{d}\sigma/\mathrm{d}z_{I\!P}$. The points show the data, the inner error bars on the points are statistical and the outer error bars show statistical and uncorrelated uncertainties added in quadrature. The correlated systematic errors are indicated by the dark band. The data are compared with predictions based on the H1 2006 Fit B DPDFs, scaled by a constant factor of 0.61, obtained using the FR (white line) and KK (dashed line) calculations. Both predictions are corrected for hadronisation effects using the factor $(1 + \delta_{hadr})$ shown below the main figure. The effect on the FR calculation of varying μ_r by factors of 0.5 and 2.0 is shown in the light band. Lower plot: ratio of the measured differential cross section to the FR calculation based on the H1 2006 Fit B DPDF set and corrected for hadronisation effects. The experimental and theory scale uncertainties are indicated as for the cross section plot. Also indicated are the central values obtained when the H1 2006 Fit A or H1 2007 Fit Jets DPDFs are used in place of H1 2006 Fit B.

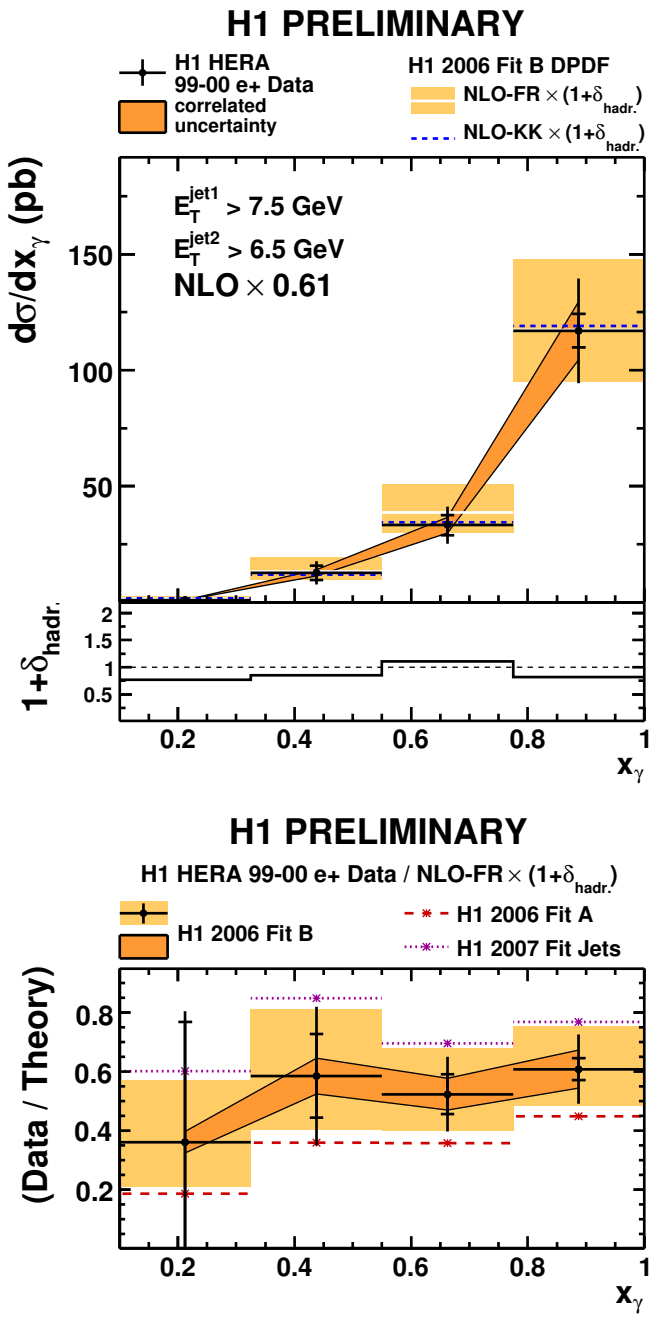

Figure 8: Upper plot: measurement of the differential cross section $\mathrm{d}\sigma/\mathrm{d}x_\gamma$. The points show the data, the inner error bars on the points are statistical and the outer error bars show statistical and uncorrelated uncertainties added in quadrature. The correlated systematic errors are indicated by the dark band. The data are compared with predictions based on the H1 2006 Fit B DPDFs, scaled by a constant factor of 0.61, obtained using the FR (white line) and KK (dashed line) calculations. Both predictions are corrected for hadronisation effects using the factor $(1 + \delta_{hadr})$ shown below the main figure. The effect on the FR calculation of varying μ_r by factors of 0.5 and 2.0 is shown in the light band. Lower plot: ratio of the measured differential cross section to the FR calculation based on the H1 2006 Fit B DPDF set and corrected for hadronisation effects. The experimental and theory scale uncertainties are indicated as for the cross section plot. Also indicated are the central values obtained when the H1 2006 Fit A or H1 2007 Fit Jets DPDFs are used in place of H1 2006 Fit B.

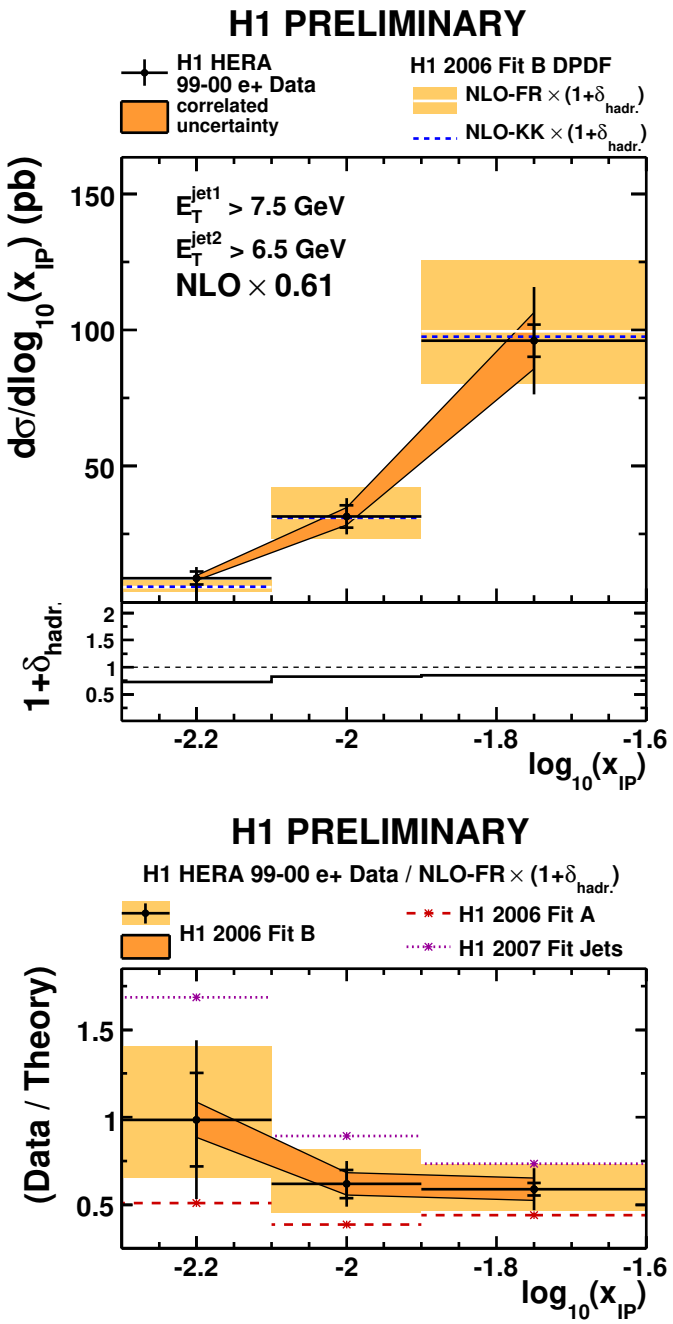

Figure 9: Upper plot: measurement of the differential cross section $\mathrm{d}\sigma/\mathrm{d}log_{10}(x_{I\!P})$. The points show the data, the inner error bars on the points are statistical and the outer error bars show statistical and uncorrelated uncertainties added in quadrature. The correlated systematic errors are indicated by the dark band. The data are compared with predictions based on the H1 2006 Fit B DPDFs, scaled by a constant factor of 0.61, obtained using the FR (white line) and KK (dashed line) calculations. Both predictions are corrected for hadronisation effects using the factor $(1+\delta_{hadr})$ shown below the main figure. The effect on the FR calculation of varying μ_r by factors of 0.5 and 2.0 is shown in the light band. Lower plot: ratio of the measured differential cross section to the FR calculation based on the H1 2006 Fit B DPDF set and corrected for hadronisation effects. The experimental and theory scale uncertainties are indicated as for the cross section plot. Also indicated are the central values obtained when the H1 2006 Fit A or H1 2007 Fit Jets DPDFs are used in place of H1 2006 Fit B.

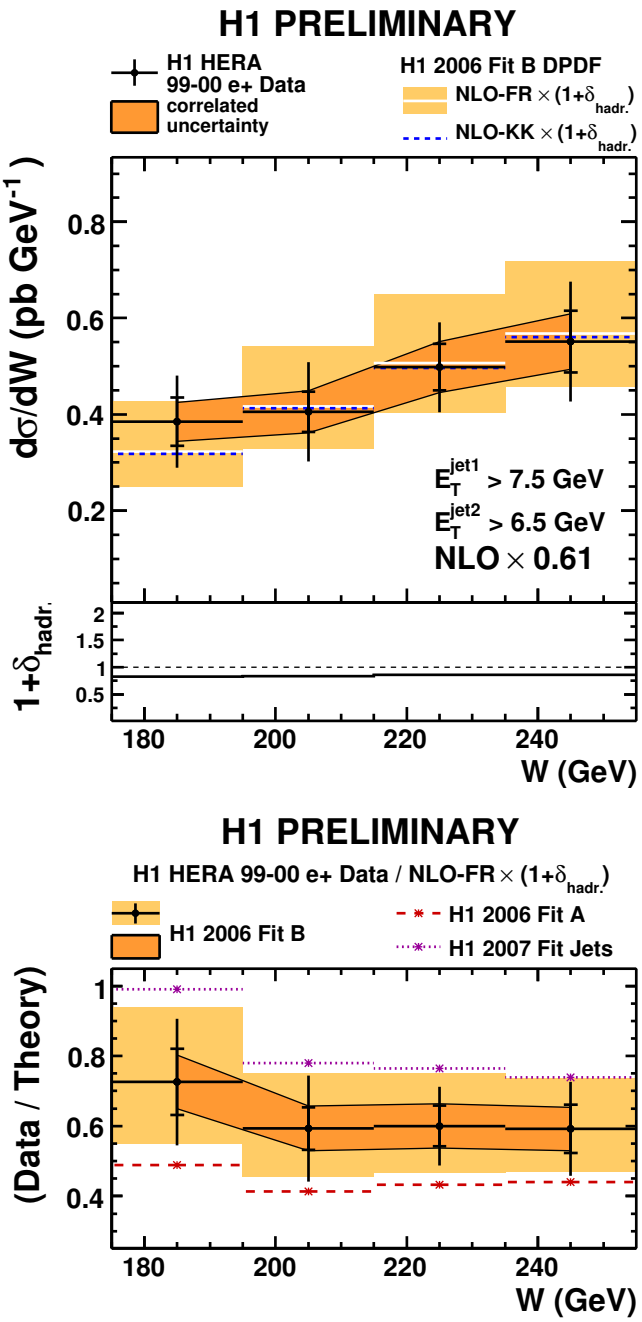

Figure 10: Upper plot: measurement of the differential cross section $\mathrm{d}\sigma/\mathrm{d}W$. The points show the data, the inner error bars on the points are statistical and the outer error bars show statistical and uncorrelated uncertainties added in quadrature. The correlated systematic errors are indicated by the dark band. The data are compared with predictions based on the H1 2006 Fit B DPDFs, scaled by a constant factor of 0.61, obtained using the FR (white line) and KK (dashed line) calculations. Both predictions are corrected for hadronisation effects using the factor $(1+\delta_{hadr})$ shown below the main figure. The effect on the FR calculation of varying μ_r by factors of 0.5 and 2.0 is shown in the light band. Lower plot: ratio of the measured differential cross section to the FR calculation based on the H1 2006 Fit B DPDF set and corrected for hadronisation effects. The experimental and theory scale uncertainties are indicated as for the cross section plot. Also indicated are the central values obtained when the H1 2006 Fit A or H1 2007 Fit Jets DPDFs are used in place of H1 2006 Fit B.

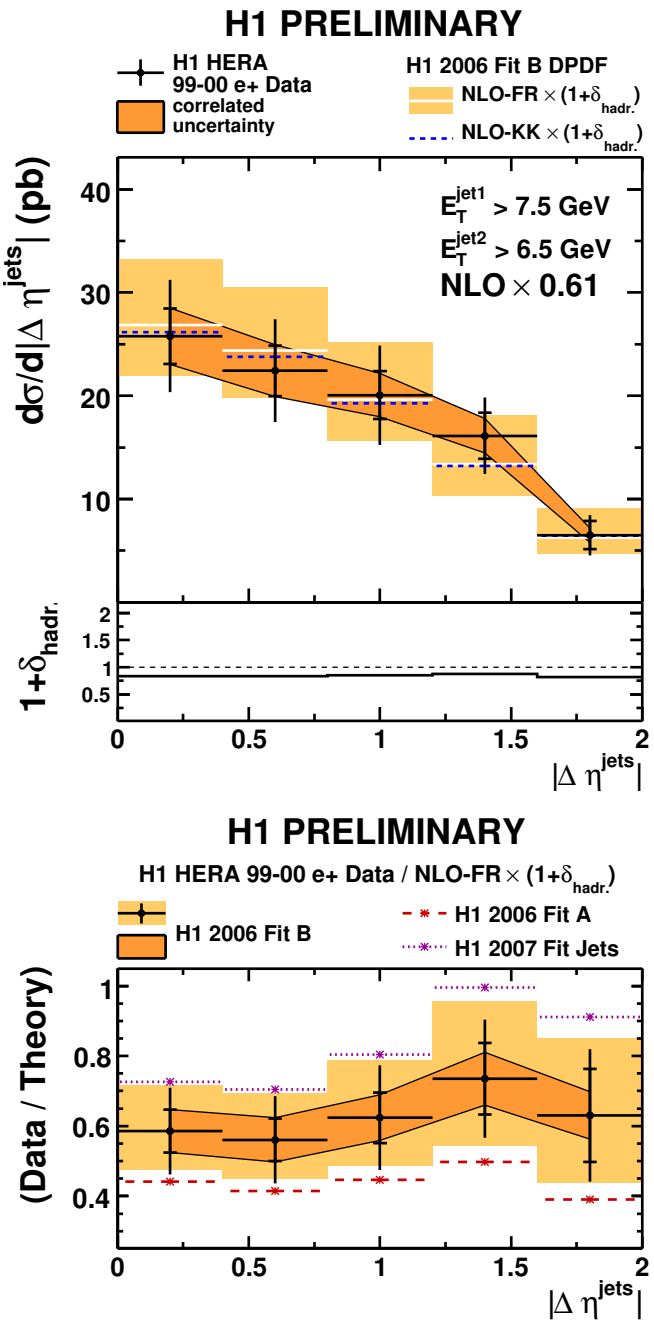

Figure 11: Upper plot: measurement of the differential cross section $\mathrm{d}\sigma/\mathrm{d}\,|\Delta\eta^{jets}|$. The points show the data, the inner error bars on the points are statistical and the outer error bars show statistical and uncorrelated uncertainties added in quadrature. The correlated systematic errors are indicated by the dark band. The data are compared with predictions based on the H1 2006 Fit B DPDFs, scaled by a constant factor of 0.61, obtained using the FR (white line) and KK (dashed line) calculations. Both predictions are corrected for hadronisation effects using the factor $(1+\delta_{hadr})$ shown below the main figure. The effect on the FR calculation of varying μ_r by factors of 0.5 and 2.0 is shown in the light band. Lower plot: ratio of the measured differential cross section to the FR calculation based on the H1 2006 Fit B DPDF set and corrected for hadronisation effects. The experimental and theory scale uncertainties are indicated as for the cross section plot. Also indicated are the central values obtained when the H1 2006 Fit A or H1 2007 Fit Jets DPDFs are used in place of H1 2006 Fit B.

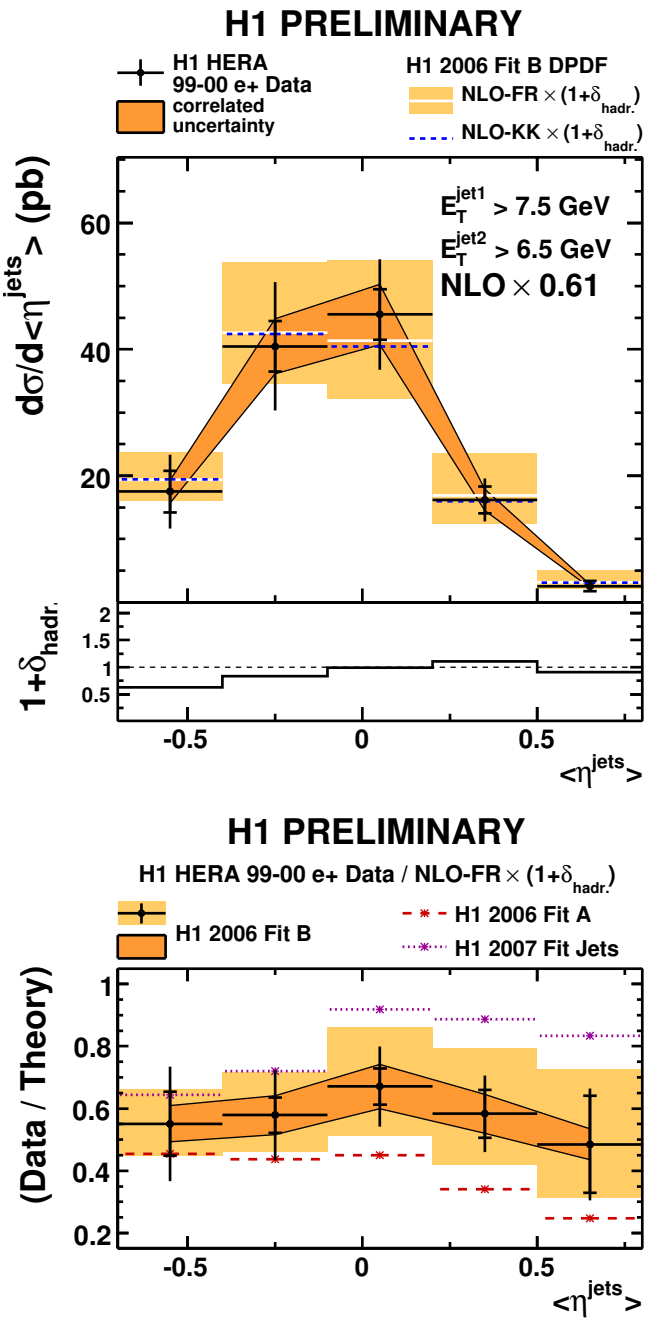

Figure 12: Upper plot: measurement of the differential cross section $\mathrm{d}\sigma/\mathrm{d}\,\langle\Delta\eta^{jets}\rangle$. The points show the data, the inner error bars on the points are statistical and the outer error bars show statistical and uncorrelated uncertainties added in quadrature. The correlated systematic errors are indicated by the dark band. The data are compared with predictions based on the H1 2006 Fit B DPDFs, scaled by a constant factor of 0.61, obtained using the FR (white line) and KK (dashed line) calculations. Both predictions are corrected for hadronisation effects using the factor $(1+\delta_{hadr})$ shown below the main figure. The effect on the FR calculation of varying μ_r by factors of 0.5 and 2.0 is shown in the light band. Lower plot: ratio of the measured differential cross section to the FR calculation based on the H1 2006 Fit B DPDF set and corrected for hadronisation effects. The experimental and theory scale uncertainties are indicated as for the cross section plot. Also indicated are the central values obtained when the H1 2006 Fit A or H1 2007 Fit Jets DPDFs are used in place of H1 2006 Fit B.

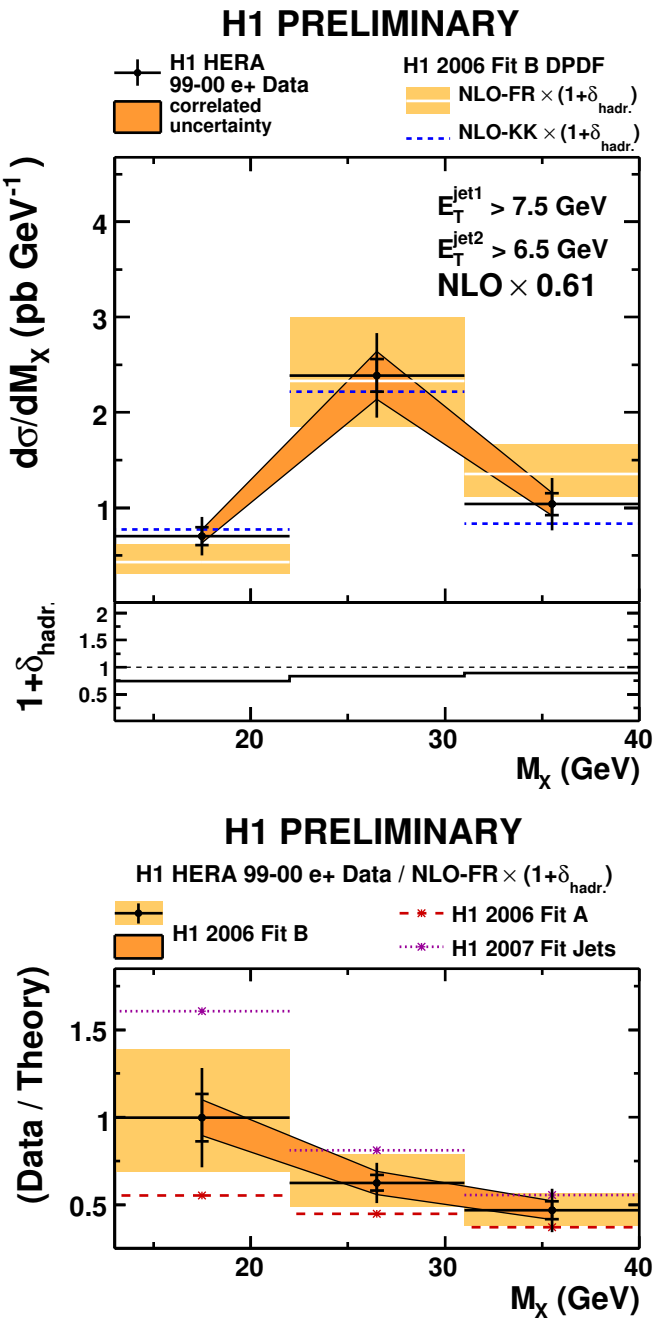

Figure 13: Upper plot: measurement of the differential cross section $\mathrm{d}\sigma/\mathrm{d}M_X$. The points show the data, the inner error bars on the points are statistical and the outer error bars show statistical and uncorrelated uncertainties added in quadrature. The correlated systematic errors are indicated by the dark band. The data are compared with predictions based on the H1 2006 Fit B DPDFs, scaled by a constant factor of 0.61, obtained using the FR (white line) and KK (dashed line) calculations. Both predictions are corrected for hadronisation effects using the factor $(1+\delta_{hadr})$ shown below the main figure. The effect on the FR calculation of varying μ_r by factors of 0.5 and 2.0 is shown in the light band. Lower plot: ratio of the measured differential cross section to the FR calculation based on the H1 2006 Fit B DPDF set and corrected for hadronisation effects. The experimental and theory scale uncertainties are indicated as for the cross section plot. Also indicated are the central values obtained when the H1 2006 Fit A or H1 2007 Fit Jets DPDFs are used in place of H1 2006 Fit B.

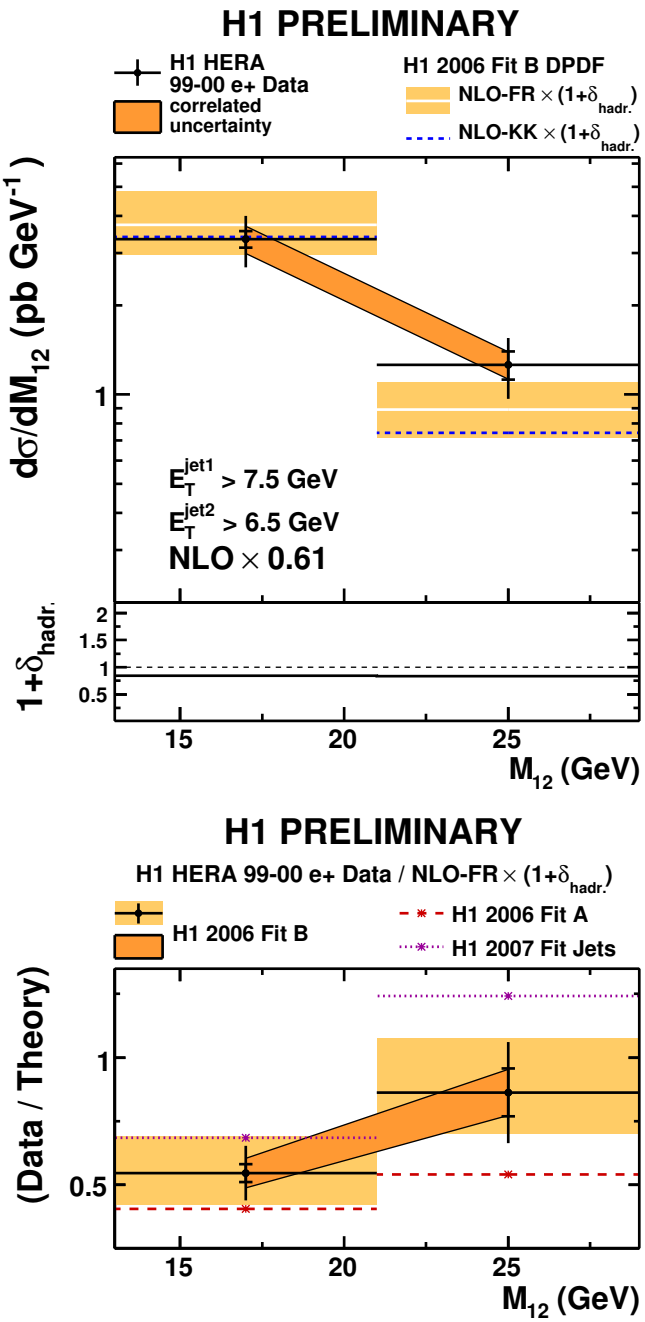

Figure 14: Upper plot: measurement of the differential cross section $\mathrm{d}\sigma/\mathrm{d}M_{12}$. The points show the data, the inner error bars on the points are statistical and the outer error bars show statistical and uncorrelated uncertainties added in quadrature. The correlated systematic errors are indicated by the dark band. The data are compared with predictions based on the H1 2006 Fit B DPDFs, scaled by a constant factor of 0.61, obtained using the FR (white line) and KK (dashed line) calculations. Both predictions are corrected for hadronisation effects using the factor $(1+\delta_{hadr})$ shown below the main figure. The effect on the FR calculation of varying μ_r by factors of 0.5 and 2.0 is shown in the light band. Lower plot: ratio of the measured differential cross section to the FR calculation based on the H1 2006 Fit B DPDF set and corrected for hadronisation effects. The experimental and theory scale uncertainties are indicated as for the cross section plot. Also indicated are the central values obtained when the H1 2006 Fit A or H1 2007 Fit Jets DPDFs are used in place of H1 2006 Fit B.